Petroleum Science 21 (2024) 4311–4327

Contents lists available at ScienceDirect

Petroleum Science

journal homepage: www.keaipublishing.com/en/journals/petroleum-science

Original Paper

Theoretical calculation and analysis of the velocity of shaped charge jet with modified collapse velocity model

Kun Jiang [a, b], Shou-Chun Deng [a, b, *], Hai-Bo Li [a, b]

[a] State Key Laboratory of Geomechanics and Geotechnical Engineering, Institute of Rock and Soil Mechanics, Chinese Academy of Sciences, Wuhan 430071, Hubei, China
[b] University of Chinese Academy of Sciences, Beijing 100049, China

ARTICLE INFO

Article history:
Received 7 September 2023
Received in revised form
28 May 2024
Accepted 25 June 2024
Available online 29 June 2024

Edited by Jia-Jia Fei and Min Li

Keywords:
Perforating shaped charge
Liner collapse velocity
Jet velocity
PER theory
Energy exploitation

ABSTRACT

The application of perforating completion technology in oil and gas field development has gained widespread popularity. Enhancing the efficiency of oil and gas wells relies on increasing the penetration depth, which is influenced by the design of the perforation charge and the strength characteristics of the rock material. However, as a crucial objective function for optimizing perforating charge structures, jet velocity lacks a rapid and accurate calculating method. This article addresses this issue by proposing an improved collapse velocity model using the DP46RDX42-Y perforating charge as a case study. It presents a novel approach for calculating jet velocity based on the unsteady Pugh-Eichelberger-Rostoker (PER) theory. To validate the effectiveness of the proposed method and analyze the impact of different characteristic parameters on jet tip velocity, a series of numerical simulations were conducted using LS-DYNA software combined with Arbitrary Lagrange-Euler (ALE) techniques. Results indicate excellent agreement between the proposed method and the numerical results, demonstrating its superiority over the traditional Gurney formula with an impressive 34.15% increase in accuracy. Notably, this method is particularly suitable for perforating charges with low detonation velocity. Increasing the liner density and decreasing the liner thickness and cone angle is recommended to achieve higher jet tip velocity. Furthermore, the proposed method has the potential for broader application in other perforating charges with varying liner shapes. This study provides a comprehensive and efficient solution for calculating jet velocity, which facilitates optimizing perforating charge structures and calculating penetration depth.

1. Introduction

The perforation charge consists of a shaped charge and a liner and is based on the theory of the shaped charge jet. The structure of the shaped charge transforms the chemical energy into the kinetic energy of the jet generated by the liners. When the high explosive detonates, the spherical shock wave compresses the liner axially and accelerates it into a continuous, high-temperature, and high-speed metal jet, which can travel at velocities ranging from 3 to 10 km/s, causing extensive damage to the target. Shaped charges have been widely used in both military (Xu et al., 2019a; Agu et al., 2018; Hu et al., 2017) and civilian applications (Xiao et al., 2017; Kolpakov et al., 2018; Yin et al., 2021), especially in oil and gas drilling (Jin and Zhang, 2020; Liu et al., 2018).

Perforating completion technology is becoming increasingly popular in shale gas exploitation (Yan et al., 2020) (see Fig. 1), which involves creating channels between the wellbore and formation using a perforating shaped charge that penetrates through the casing, cement sheath and formation sequentially (Liu et al., 2018). The shape and volume of the formed perforations can impact subsequent fracturing effects. Typically, the oil and gas well production is determined by the maximum penetration depth of the shaped charge jet into the target, which is then used to evaluate the charge efficiency (Mu et al., 2022). The efficiency of oil and gas wells can be enhanced by increasing the penetration depth, which is dictated by the design of the perforation charge and the strength of the rock material (Elshenawy and Li, 2013). Allison and Vitali (1963) developed three distinct models for charge jet penetration by assuming the existence of a virtual origin (VO) within the charge. The formula below can be used to calculate the penetration depth

* Corresponding author.
E-mail address: scdeng@whrsm.ac.cn (S.-C. Deng).

https://doi.org/10.1016/j.petsci.2024.06.017

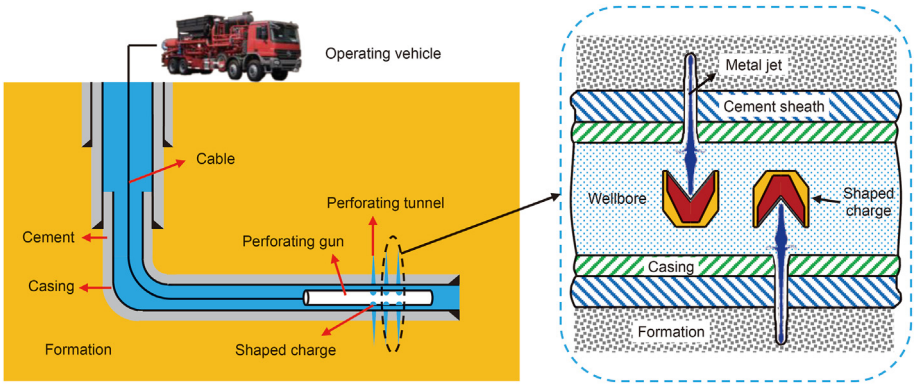

Fig. 1. Perforating completion in oil and gas exploitation.

of the continuous jet:

$$H = Z\left(\left(\frac{V_j}{V_c}\right)^{\frac{1}{\gamma}} - 1\right) \tag{1}$$

where Z is the effective jet length measured from VO to the target; V_j and V_c are the jet tip and rear velocity, respectively; γ is the square root of the target-jet density ratio, $\gamma = \sqrt{\rho_T/\rho_j}$. The mentioned model has gained widespread acceptance and can be utilized to predict the penetration depth (Agu et al., 2018; Elshenawy et al., 2018). The velocity of metal jets plays a crucial role in penetrating reservoirs.

The jet velocity formed by shaped charges has been extensively studied through theoretical, experimental, and numerical methods. Birkhoff et al. (1948) developed a theory of steady jet forming by assuming that the liner was a non-viscous, incompressible fluid. However, neglecting the strength of the liner, this theory cannot accurately predict the velocity gradient and mass distribution of the jet and slug. To address this, Pugh et al. (1952) proposed a classic unsteady state PER theoretical model that suggests the collapse velocity of the liner gradually decreases from the top to the bottom. Researchers have continuously validated and improved the PER theory. Allison and Vitali (1963) used radioactive tracer technology to validate the PER model. Perez et al. (1977) calculated the two-dimensional flow effect near the axis of liners during the collapse process. Hirsch (1979) added the unsteady effects of collision and jet formation points. Chou et al. (1983) improved the Gurney velocity formula and proposed a new formula for calculating the collapse velocity and Taylor angle. Curtis and Kelly (1994) proposed a cylindrical flow model for jet and slug under asymmetric conditions using the variational method. Sun et al. (2009) introduced the acceleration of the liner element to reflect the acceleration collapse process and calculate the jet shape. Chen et al. (2015) utilized the Mach and normal oblique reflection pressures generated from the collision of detonation waves to calculate the collapse velocity of the liner and incorporated it into the PER theory to establish a model for the formation of a rod-like jet. Shi et al. (2023) predicted jet formation using the relationship between stagnation pressure and two critical pressures, avoiding using collapse angles that are difficult to measure accurately. In terms of measuring jet velocity, there are two methods: electromagnetic coil (Ayisit, 2008) and X-ray technology (Shi et al., 2023; Yavuz et al., 2012).

Numerical simulation is more cost-effective and time-efficient than other methods when simulating shaped charge perforating charges. Various numerical methods have been introduced in recent decades. Chen and Liu (2012) proposed a Euler algorithm to simulate the formation of metal jets, and the numerical results are highly consistent with experimental data. Nie et al. (2014) analyzed near-surface explosions using the finite volume method (FVM). Ge et al. (2023) uses 2D Euler encoding technology to design shaped charges of truncated conical hyperaccumulation. Agu et al. (2018) simulated the detonation of the shaped charge using ANSYS AUTODYA. Liu et al. (2018) used LS-DYNA software, combined with ALE and Adaptive Mesh Refinement (AMR) techniques, to establish a pressure field model for oil and gas wells during the jet process. Xu et al. (2023a) developed a Eulerian Finite Element Method (EFEM) based on the Volume of fluid (VOF) method to simulate underwater explosions of hypervelocity-shaped charge. Grid-based methods struggle with shaped charge explosions due to mesh distortion and numerical instability caused by large deformations. Recently, meshless methods such as the Material Point Method (MPM) (Xu et al., 2023b) and Smooth Particle Hydrodynamics (SPH) (Zhang et al., 2017; Wu et al., 2022; Chen et al., 2020) have been more effective in solving such problems. However, choosing parameters such as particle spacing and smoothing length can seriously impact simulation accuracy and stability (Ma et al., 2009). So, it is imperative to develop a method for calculating the velocity of the jet produced by perforating charges under different conditions (explosives, liners, shaped charge structures, etc.).

This article, built upon the unsteady PER theory, improved the collapse velocity model and introduced a novel approach for calculating jet velocity. Subsequently, through simulation using the nonlinear finite element software LS-DYNA combined with ALE techniques, the formation of the jet was analyzed. The impact of various characteristic parameters on jet velocity was assessed, and a comparison between numerical and calculated results was conducted. The results are in agreement, showing the accuracy and applicability of the proposed method.

2. Theoretical calculations

2.1. Formation theory of shaped charge jet

Theoretical analysis shows that the formation process of shaped charge jets can be divided into the following three stages: explosive detonation, the collapse of the liner, and the formation of jet and slug, as shown in Fig. 2.

Firstly, when an explosive is detonated at its initiation point, the energy of the detonation product accumulates at the opposite end of the liner. Currently, most models that predict jet formation use detonation velocity (V_d) to replace the characteristics of explosives

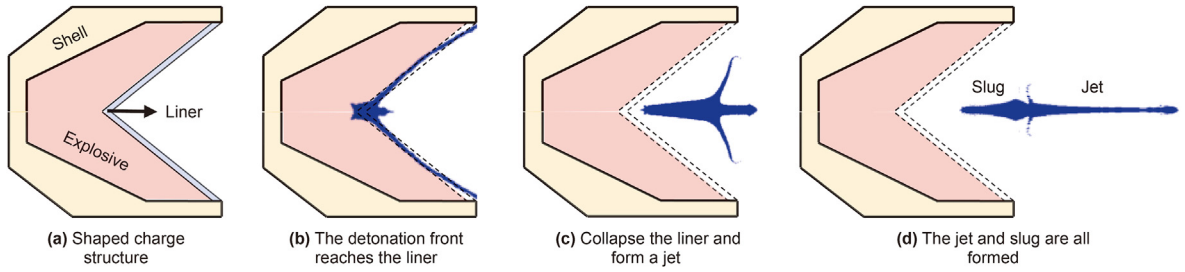

Fig. 2. Shaped charge structure and formation process of the jet.

without modeling or analyzing their detonation process. As shown in Fig. 4, the detonation wave propagates with velocity (V_d), sweeping through the charge liner at a velocity that is tangent to the liner when the front reaches it. Then, when the detonation wave propagates on the liner, the liner element moves to the axis with the velocity V_0. In the unsteady PER model, the liner elements are assumed to accelerate to the liner axis instantaneously, and the collapse velocity decreases from the top to the bottom of the liner. Finally, under the detonation wave, the liner elements converge to the symmetrical axis, and the formed jet elements only move along the axis. During the process, the jet with higher velocity forms the head, while the part with lower velocity forms the slug.

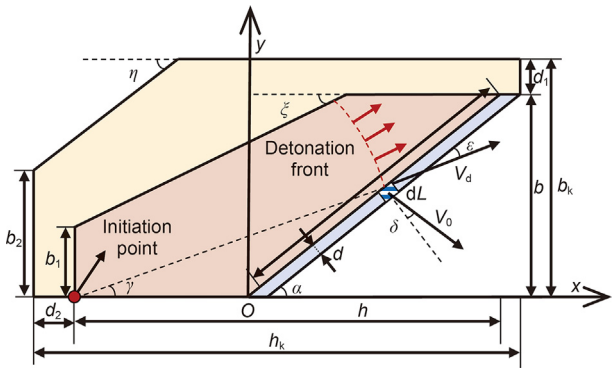

Fig. 4. Calculation model of shaped charge.

2.2. PER model

Pugh-Eichelberger-Rostoker (PER) model is suitable for describing liner collapse, where collapse velocity gradually decreases from top to bottom. Fig. 3 describes the state of each element of the liner during collapse. OPQ is the initial state of the liner, P and P′ are the liner elements, V_0 is the collapse velocity, U_d is the horizontal component of the detonation velocity (V_d), β is the collapse angle.

When the detonation wave moves along the OPQ, the liner element at point P collapses to point J. In the steady model, P′ collapses to N, but in the PER model, P′ can only reach M, resulting in the collapse curve being JMQ rather than JNQ. The collapse angle increases gradually along the liner, $\beta > \beta' = \alpha + 2\delta$. δ is the Taylor deflection angle.

The coordinate system is established at the collision point between the detonation wave and the liner element. Fig. 3(b) depicts the relationship between the flow velocity of the liner element (V_2), convergence velocity of the liner element (V_1), and collapse velocity (V_0). According to the law of sines, V_1 and V_2 can be obtained by

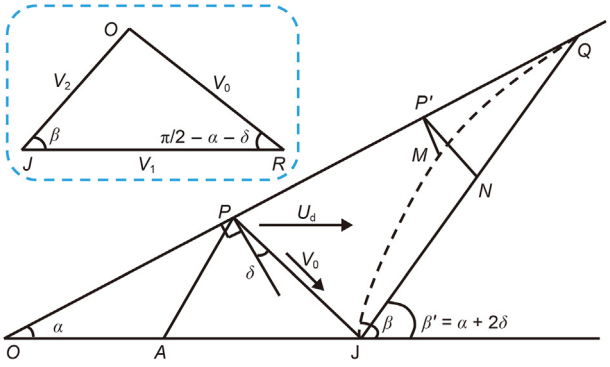

Fig. 3. Schematic diagram of the collapse process of the liner.

$$\begin{cases} V_1 = \dfrac{V_0}{\sin\beta}\sin\left(\dfrac{\pi}{2} - \beta + \alpha - \delta\right) = \dfrac{V_t}{\sin\beta}\cos(\beta - \alpha + \delta) \\ V_2 = \dfrac{V_0}{\sin\beta}\sin\left(\dfrac{\pi}{2} - \alpha - \delta\right) = \dfrac{V_t}{\sin\beta}\cos(\alpha + \delta) \end{cases} \tag{2}$$

The velocities of the jet and slug can be written as

$$\begin{cases} V_j = V_1 + V_2 = \dfrac{V_0}{\sin(\beta/2)}\cos(\alpha + \delta - \beta/2) \\ V_s = V_1 - V_2 = \dfrac{V_0}{\cos(\beta/2)}\sin(\alpha + \delta - \beta/2) \end{cases} \tag{3}$$

According to the conservation of mass and momentum, the element mass of the liner can be obtained:

$$\begin{cases} dm = dm_j + dm_s \\ dmV_s\cos\beta = -dm_jV_2 + dm_sV_2 \end{cases} \tag{4}$$

where dm_j, dm_s are the element mass of jet and slug, which can be written as:

$$\begin{cases} dm_j = \dfrac{1}{2}(1 - \cos\beta)dm = \sin^2\left(\dfrac{\beta}{2}\right)dm \\ dm_s = \dfrac{1}{2}(1 - \sin\beta)dm = \cos^2\left(\dfrac{\beta}{2}\right)dm \end{cases} \tag{5}$$

2.3. Calculation of jet parameter

From Eqs. (2) and (5), it can be inferred that to obtain the velocity and mass of the jet and slug, it is necessary to know the collapse velocity, deflection angle, collapse angle, and mass of the liner microelement, and solve them in conjunction with the specific

structure of the perforated charge. The solution approach for the characteristic parameters of jet forming is as follows:

2.3.1. Shaped charge structure

Establish a 2D geometric model using the DP46RDX42-Y perforating charge. Due to the axial symmetry of the structure, the half structure can be selected for research, with the axis as the *X*-axis and the radial radius as the *Y*-axis. At the same time, cylindrical coordinates (r, z) are used, as shown in Fig. 4. The liner is divided into N microelements, where i is the i-th microelement. The effective length of the liner element is:

$$\mathrm{d}L = \frac{L}{N} = \frac{b\csc\alpha - d\cot\alpha}{N} \tag{6}$$

The initial position of the liner element can be expressed as follows

$$\begin{cases} x_i = (i\mathrm{d}L + d\cot\alpha)\cos\alpha \\ y_i = x_i\tan\alpha \end{cases} \tag{7}$$

From the previous section, it can be seen that the jet velocity, slug velocity, jet mass, and slug mass of the element are as follows, respectively:

$$\begin{cases} V_{ji} = V_{0i}\csc(\beta_i/2)\cos(\alpha+\delta_i-\beta_i/2) \\ V_{si} = V_{0i}\sec(\beta_i/2)\sin(\alpha+\delta_i-\beta_i/2) \\ \mathrm{d}m_{ji} = \sin^2(\beta_i/2)\mathrm{d}m_i \\ \mathrm{d}m_{si} = \cos^2(\beta_i/2)\mathrm{d}m_i \end{cases} \tag{8}$$

The known structural dimensions and material parameters are as follows: ρ_e is the charge density; ρ_m is the liner density; ρ_k is the shell density; b is the half width of explosive; b_k is the half width of shell; b_1 is the top half width of explosive; b_2 is the top half width of shell; h is the height of explosive; h_k is the height of shell; α is the half cone angle of liner; ξ is the explosive angle; η is the shell angle; ε is the angle between the detonated velocity vector and the tangent line of the liner; γ is the angle between the detonated velocity vector and the axis of the liner; d is the liner thickness; d_1, d_2 are the shell thickness of different cross-sections; L is the effective length of liner; V_d is the detonated velocity of explosive.

2.3.2. Collapse velocity

In the PER model, the number of unknown variables exceeds the number of independent equations, and collapse velocity must be determined in advance by other methods to close the equations.

2.3.2.1. Gurney formula. The Gurney formula is commonly used to analyze and solve the collapse velocity of the liner. It assumes that all the potential energy of the explosive is converted into the kinetic energy of the metal and the explosive product. The formula depends on the mass ratio of the explosive to the liner and the Gurney characteristic velocity. The velocity expression is as follows (Gurney, 1943):

$$V = \sqrt{2E}\left(\frac{(1+2M/C)^3+1}{6(1+M/C)} + \frac{M}{C}\right)^{-1/2} \tag{9}$$

where E is the Gurney energy, which is the chemical energy in the initial state of the explosive, converted into kinetic energy during detonation. In addition, for the sandwich structure, M and C represent the mass per unit area of metal and explosive; for the cylindrical structure, they represent the mass per unit length of metal and explosive; for the spherical structures, they represent the mass per unit volume of metal and explosive. Chou et al. gave a simplified formula to calculate the collapse velocity of a liner for a cylindrical charge (Chou and Flis, 1986; Chou et al., 1976), where $\mu = C/M$.

$$V_0 = \sqrt{2E\frac{3\mu^2}{\mu^2+5\mu+4}} \tag{10}$$

Based on Fig. 5, we calculate the mass ratio of explosive to liner under this geometric model.

$$\mu = C_i / M_i = \rho_e d_{ei} / (\rho_m d + \rho_k d_{ki}) \tag{11}$$

where d_{ei} and d_{ki} are the explosive and shell thickness corresponding to the liner element, respectively.

First, solve the explosive thickness corresponding to the liner element (d_{ei}). L_{me} is the projection of the outer normal of the top of the liner on the extension line of the top of the explosive, $L_{me} = (h - b\cot\alpha + d\csc\alpha)\cot\alpha$; b_1 is the top half width of the explosive; L_{le} is the projection of the outer normal of the liner passing through the point A on the extension line at the top of the explosive, $L_{le} = (b - b_1)\cot\xi\cot\alpha + b$. There are three possible situations for calculating d_{ei} based on the sizes of L_{me}, b_1, and L_{le}:

when $L_{me} > L_{le}$,

$$d_{ei} = d_{ei0} = (L - i\mathrm{d}L)\tan\alpha \tag{12}$$

when $b_1 < L_{me} < L_{le}$,

$$d_{ei} = \begin{cases} (L - i\mathrm{d}L)\tan\alpha & L - i\mathrm{d}L < L_1 \\ d_{ei0} - (d_{ei0} - h_1)\csc(\pi/2 - \xi + \alpha)\sin\xi & L - i\mathrm{d}L > L_1 \end{cases} \tag{13}$$

when $L_{me} < b_1$,

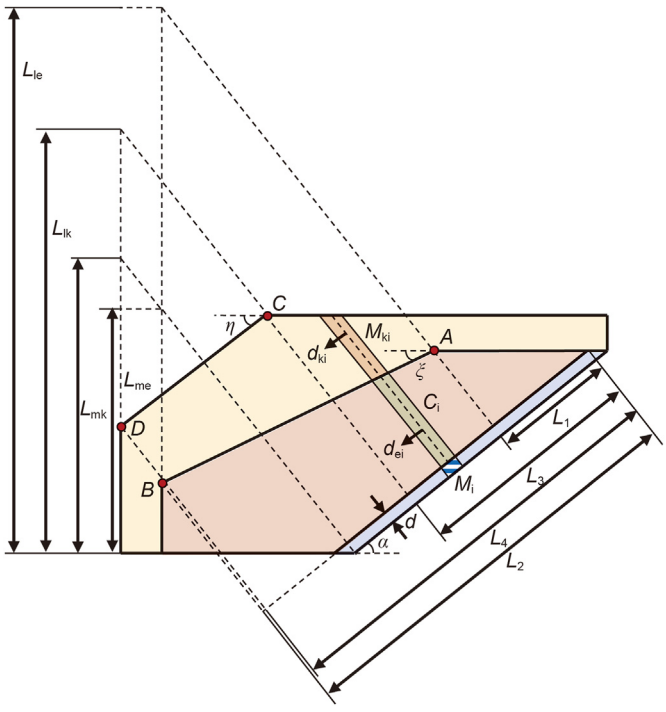

Fig. 5. Calculation model schematic of liner collapse velocity (Gurney velocity method).

$$d_{ei}=\begin{cases}(L-\mathrm{id}L)\tan\alpha & L-\mathrm{id}L<L_1\\ d_{ei0}-(d_{ei0}\csc\alpha-h_1)\csc(\pi/2-\xi+\alpha)\sin\xi & L_1<L-\mathrm{id}L<L_2\\ d_{ei0}-(d_{ei0}\csc\alpha-h)\csc\alpha & L-\mathrm{id}L>L_2\end{cases} \tag{14}$$

where L_1 is the projection of point A in the tangent direction of the liner, $L_1 = h_1\cos\alpha$; L_2 is the projection of point B in the tangent direction of the liner, $L_2 = (h+(b-b_1)\tan\alpha)\cos\alpha$; h_1 is the height of the side wall of the explosive, $h_1 = h-(b-b_1)\cot\alpha$.

Then, solve the shell thickness corresponding to the liner element (d_{ki}). L_{mk} is the outer normal of the top of the liner on the extension line of the top of the shell, $L_{\mathrm{mk}} = (h+d_2-b\cot\alpha+d\csc\alpha)\cot\alpha$; b_2 is the top half width of the shell; L_{lk} is the projection of the outer normal of the liner passing through the point C on the extension line at the top of the explosive, $L_{\mathrm{lk}} = (b_{\mathrm{k}}-b_2)\cot\eta\cot\alpha+b_{\mathrm{k}}$. There are three possible situations for calculating d_{ki} based on the sizes of L_{mk}, b_2, and L_{lk}:

when $L_{\mathrm{mk}}>L_{\mathrm{lk}}$,

$$d_{\mathrm{ki}}=(d_1\csc\alpha+L-\mathrm{id}L)\tan\alpha-d_{ei} \tag{15}$$

when $b_2<L_{\mathrm{mk}}<L_{\mathrm{lk}}$,

$$d_{\mathrm{ki}}=\begin{cases}(d_1\csc\alpha+L-\mathrm{id}L)\tan\alpha-d_{ei} & L-\mathrm{id}L+d_1\csc\alpha<L_3\\ d_{ki0}-(d_{ki0}\csc\alpha-h_2)\csc(\pi/2-\eta+\alpha)\sin\eta-d_{ei} & L-\mathrm{id}L+d_1\csc\alpha>L_3\end{cases} \tag{16}$$

where $d_{ki0} = d_1\csc\alpha+(L-\mathrm{id}L)\tan\alpha$.

When $L_{\mathrm{mk}}<b_2$,

$$d_{\mathrm{ki}}=\begin{cases}(d_1\csc\alpha+L-\mathrm{id}L)\tan\alpha-d_{ei} & L-\mathrm{id}L+d_1\csc\alpha<L_3\\ d_{ki0}-(d_{ki0}\csc\alpha-h_2)\csc(\pi/2-\eta+\alpha)\sin\eta-d_{ei} & L_3<L-\mathrm{id}L+d_1\csc\alpha<L_4\\ d_{ki0}-(d_{ki0}\csc\alpha-h_{\mathrm{k}}+d\csc\alpha-d_1\cot\alpha)\csc\alpha-d_{ei} & L-\mathrm{id}L+d_1\csc\alpha>L_4\end{cases} \tag{17}$$

where L_3 is the projection of point C in the tangent direction of the liner, $L_3 = h_2\cos\alpha$; L_4 is the projection of point D in the tangent direction of the liner, $L_4 = ((b_{\mathrm{k}}-b_2)\tan\alpha+h_{\mathrm{k}}-(d\csc\alpha-d_1\cot\alpha))\cos\alpha$; h_2 is the height of the shell, $h_2 = h_{\mathrm{k}}-(b_{\mathrm{k}}-b_2)\cot\eta-(d\csc\alpha-d_1\cot\alpha)$.

2.3.2.2. Velocity decomposition. The above calculation method cannot comprehensively consider the influence of many factors on the collapse velocity, and the process is complex. Chou et al. (1986) presents a simple and effective method for calculating collapse velocity, considering the influence of liner, shell, explosive, and shaped charge structure.

Fig. 6 illustrates the model for calculating the velocity of liner collapse. The liner is affected by explosives in both radial and axial directions. So, the collapse velocity could be expressed as

$$\begin{cases}V_{0i}=f(\varphi_i)V_{\mathrm{pi}}+g(\varphi_i)V_{ci}\\ f(\varphi_i)=1-\sin\varphi_i\\ g(\varphi_i)=\sin\varphi_i\end{cases} \tag{18}$$

where φ_i is the angle between the line, which connects the position of the liner element and the horizontal projection point of the liner bottom, and the axis of symmetry,

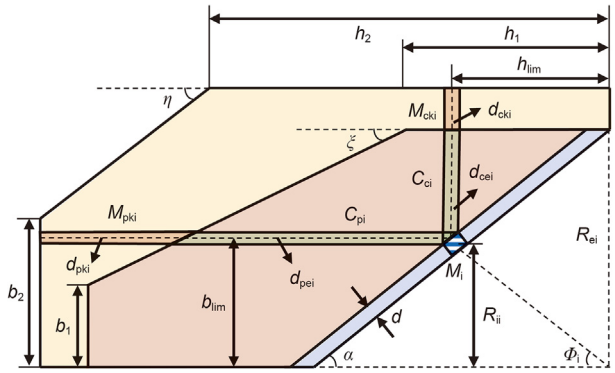

Fig. 6. Calculation model schematic of liner collapse velocity (Decomposition velocity method).

$$\tan\varphi_i=\frac{(\mathrm{id}L+d\cot\alpha)\sin\alpha}{b\cot\alpha+d\csc\alpha-(\mathrm{id}L+d\cot\alpha)\cos\alpha} \tag{19}$$

where V_{pi} and V_{ci} are the collapse velocity component of the axial and the radial liner element.

$$\begin{cases}V_{\mathrm{pi}}=\sqrt{2E}\left(\dfrac{(1+2R_{\mathrm{pi}})^3+1}{6(1+R_{\mathrm{pi}})}+R_{\mathrm{pi}}\right)^{-1/2}\\ V_{ci}=\sqrt{2E}\left(\dfrac{R_{\mathrm{ei}}^2-R_{\mathrm{ii}}^2}{R_{\mathrm{xi}}^2-R_{\mathrm{ii}}^2}R_{ci}+\dfrac{1}{6}\right)^{-1/2}\end{cases} \tag{20}$$

where E is the Gurney energy of the explosive, which can be obtained from the following formula (Shen et al., 2013),

$$E=\frac{1}{2}\left(\frac{GV_{\mathrm{d}}\cos\gamma}{\gamma_{\mathrm{CJ}}+1}\right)^2 \tag{21}$$

where G is the Gurney coefficient, which can be taken as 1.32, γ_{CJ} is the adiabatic index,

$$\gamma_{\mathrm{CJ}}=1.25+\frac{1.42\rho_0}{1+0.27\rho_0}+0.1n \tag{22}$$

where ρ_0 is the initial explosive density; n is the number of carbonyl groups contained in the structural formula of the explosive.

In addition, R_{ii} and R_{ei} are the interior and exterior radius of the explosive corresponding to the liner element, respectively, $R_{ei} = R_{ii} + d_{cei}$, $R_{ii} = b - (L - idL)\sin\alpha$; R_{xi} is the assumed radius of the rigid surface of the explosive, which was obtained by assuming that there is an immovable cylinder surface in the explosive (Chanteret, 1983):

$$R_{xi}^3 + 3R_{xi}\left((R_{ei}+R_{ii})\frac{\rho_0}{\rho_{CJ}}(R_{ci}R_{ei}+R_{ki}R_{ii}) + R_{ii}R_{ei}\right) - 3(R_{ei}+R_{ii})R_{ii}R_{ei}\left(\frac{2}{3}\frac{\rho_0}{\rho_{CJ}}(R_{ci}+R_{ki})\right) = 0 \tag{23}$$

where R_{pi} is the mass ratio of the liner to explosive in the axial direction; R_{ci} is the mass ratio of the liner to explosive in the radial direction,

$$d_{pei} = \begin{cases} h - b\cot\alpha + b_{lim}\cot\alpha & b_{lim} < b_1 \\ h - b\cot\alpha + b_{lim}\cot\alpha - (b_{lim} - b_1)\cot\xi & b_1 < b_{lim} < b \end{cases} \tag{25}$$

Similarly, h_{lim} is the axial projection of the position of the liner element, $h_{lim} = (L - idL)\cos\alpha$; h_1 is the height of the side wall of the explosive, $h_1 = h - (b - b_1)\cot\xi$. There are two possible situations for calculating d_{cei} based on the sizes of h_{lim} and h_1:

$$d_{cei} = \begin{cases} h_{lim}\tan\alpha & h_{lim} < h_1 \\ h_{lim}\tan\alpha - (h_{lim} - h_1)\tan\xi & h_1 < h_{lim} < h \end{cases} \tag{26}$$

Then, solve the axial and radial shell thickness (d_{pki}, d_{cki}). There are three possible situations for calculating d_{pki} based on the sizes of b_{lim}, b_1 and b_2:

$$d_{pki} = \begin{cases} d_2 & b_{lim} < \min(b_1, b_2) \\ d_2 + (b_{lim} - \min(b_1, b_2))\cot\xi & \min(b_1, b_2) < b_{lim} < \max(b_1, b_2) \\ d_2 + (b_{lim} - b_1)\cot\xi - (b_{lim} - b_2)\cot\eta & \max(b_1, b_2) < b_{lim} < b \end{cases} \tag{27}$$

Similarly, h_1 and h_2 are the height of the side wall of the explosive and shell: $h_1 = h - (b - b_1)\cot\xi$; $h_2 = h_k - (b - b_2)\cot\eta$. There are three possible situations for calculating d_{cki} based on the sizes of h_{lim}, h_1 and h_2:

$$d_{cki} = \begin{cases} d_1 & h_{lim} < \min(h_1, h_2) \\ d_1 + (h_{lim} - \min(h_1, h_2))\tan\xi & \min(h_1, h_2) < h_{lim} < \max(h_1, h_2) \\ d_1 + (h_{lim} - h_1)\tan\xi - (h_{lim} - h_2)\tan\eta & \max(h_1, h_2) < h_{lim} < h \end{cases} \tag{28}$$

$$\begin{cases} R_{pi} = \dfrac{M_i}{C_{pi}} = \dfrac{\rho_m d_i}{\rho_e d_{pei} + \rho_k d_{pki}} \\ R_{ci} = \dfrac{M_i}{C_{ci}} = \dfrac{\rho_m d_i}{\rho_e d_{cei} + \rho_k d_{cki}} \\ R_{ki} = \dfrac{M_{ki}}{C_{ci}} = \dfrac{\rho_k d_{cki}}{\rho_e d_{cei}} \end{cases} \tag{24}$$

where C_{pi} is the mass of the axial explosive corresponding to the liner element due to plate acceleration, M_i is the mass of the liner element, d_{pei} and d_{pki} are the thickness of the axial explosive and the shell corresponding to the liner element, C_{ci} is the mass of radial explosive corresponding to the liner element due to cylindrical implosion, d_{cei} and d_{cki} are the thickness of radial explosive and the shell corresponding to the liner element, M_{ki} is the shell mass corresponding to the liner elements, ρ_0 and ρ_{CJ} are the initial density and CJ density of the explosive, respectively.

The following is based on Fig. 6 to solve the axial and radial explosive and shell thickness corresponding to the liner element.

First, solve the axial and radial explosive thickness (d_{pei}, d_{cei}). b_{lim} is the radial projection of the position of the liner element, $b_{lim} = (idL + d\cot\alpha)\sin\alpha$; b_1 is the half width of the explosive. There are two possible situations for calculating d_{pei} based on the sizes of b_{lim} and b_1:

2.3.3. Deflection angle

δ_i is the element deflection angle of the liner, which can be obtained by the Taylor formula,

$$\delta_i = \arcsin\left(\frac{V_{0i}\cos\varepsilon_i}{2V_d}\right) \tag{29}$$

where ε_i is the angle between the detonation velocity vector and the tangent of the liner, $\varepsilon_i = \alpha - \gamma_i$; γ_i is the angle between the detonated velocity vector and the axis of the liner,

Table 1
Parameters of perforating charge.

Parameter	Value	Parameter	Value
b, cm	2.3	h, cm	5.6
b_1, cm	1	h_k, cm	6.1
b_k, cm	1	ρ_e, kg/m^3	1.82
b_2, cm	2.6	ξ, °	18
η, °	40	d_1, cm	0.3
V_d, cm/μs	0.848	d_2, cm	0.5
α, °	35	ρ_d, kg/m^3	8.96
d, cm	0.1	ρ_{ek}, kg/m^3	7.86

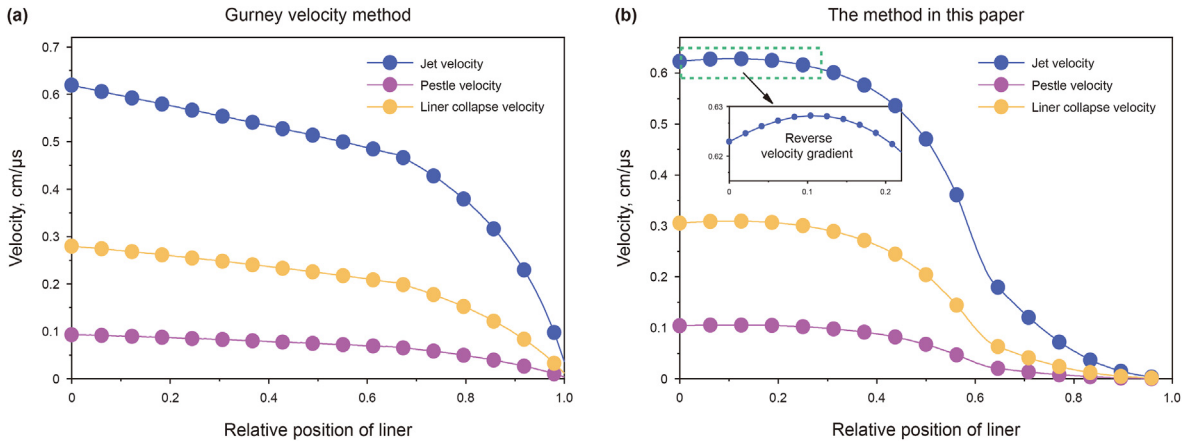

Fig. 7. The jet, slug, and collapse velocity distribution under different calculation methods.

$$\gamma_i = \arctan\left(\frac{y_i}{h - b\cot\alpha + x_i}\right) \tag{30}$$

2.3.4. Collapse angle

In the unsteady theory, it is necessary to calculate the collapse angle β_i in real time because the collapse velocity of jet microelements varies with their position. According to Fig. 4, the real-time position of the liner element in cylindrical coordinates (r, z) can be determined using the previously obtained collapse velocity V_{0i} and deflection angle δ_i:

$$\begin{cases} r_i = x_i\tan\alpha - V_{0i}(t - t_{0i})\cos(\alpha + \delta_i) \\ z_i = x_i + V_{0i}(t - t_{0i})\sin(\alpha + \delta_i) \end{cases} \tag{31}$$

where t_{0i} is the time from the initiation of the explosive to the i-th microelement,

$$t_{0i} = \frac{\sqrt{(x_i + h - b\cot\alpha)^2 + (x_i\tan\alpha)^2}}{V_d} \tag{32}$$

When the liner element reaches the axis, $r_i = 0$, then

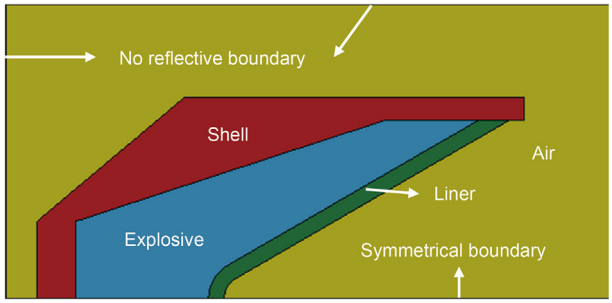

Fig. 9. Numerical simulation model of shaped charge and boundary settings.

Table 2
Four variables that change in numerical models.

Liner cone angle α, °	Liner thickness d, mm	Liner material	Explosive type
50	0.5	Copper	TNT
60	1.0	Steel	OCTOL
70	1.5	Titanium	B explosive
80	2.0	Tungsten	C-1 explosive
			8701 explosive

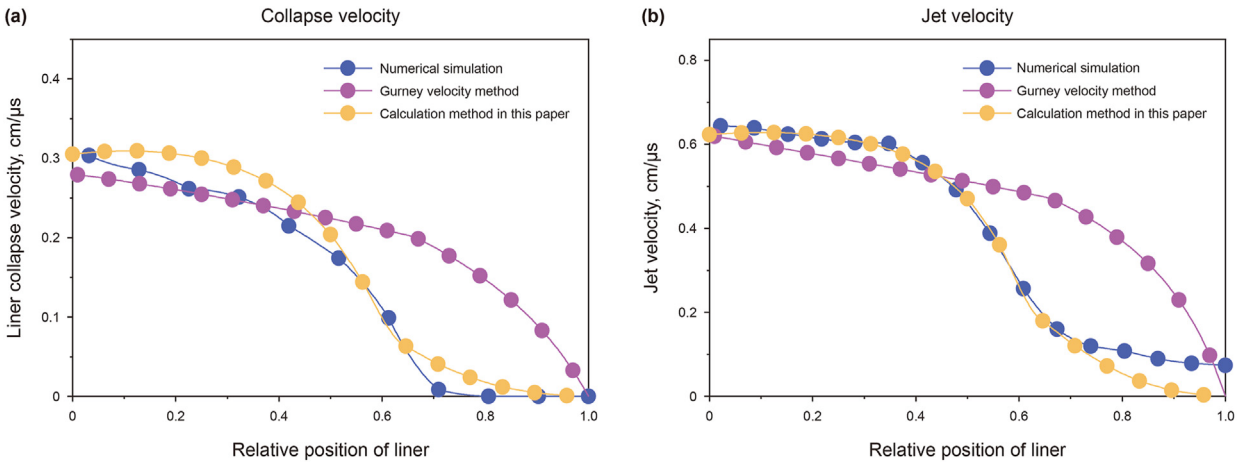

Fig. 8. Comparison of velocity distribution calculated by two theories.

$$t - t_{0i} = \frac{x_i \tan\alpha}{V_{0i}\cos(\alpha + \delta_i)} \tag{33}$$

The slope of the curve JMQ (See Fig. 3) composed of all micro-elements at the intersection of the axes is tan β_i:

$$\tan\beta_i = \frac{\partial r}{\partial z}|_{r=0} = \frac{\partial r}{\partial x} \Big/ \frac{\partial z}{\partial x}|_{r=0} = \frac{\tan\alpha - V'_{0i}(t-t_{0i})\cos(\alpha+\delta_i) + V_{0i}t'_{0i}\cos(\alpha+\delta_i) + V_{0i}(t-t_{0i})\sin(\alpha+\delta_i)\delta'_i}{1 + V'_{0i}(t-t_{0i})\sin(\alpha+\delta_i) - V_{0i}t'_{0i}\sin(\alpha+\delta_i) + V_{0i}(t-t_{0i})\cos(\alpha+\delta_i)\delta'_i} \tag{34}$$

where V'_{0i}, t'_{0i}, and δ'_i represent the partial derivatives of x, and the collapse angle of the element β_i can be obtained using the arctangent.

2.4. Example results and analysis

Jet characteristics were calculated for the DP46RDX42-Y shaped charge using the methods mentioned above. The material and geometric parameters of the perforating charge are shown in Table 1.

Fig. 7 shows the distribution of jet, slug, and collapse velocity along the liner. Two methods were used to obtain the results, showing the same trend of velocity change. The jet parameters decrease as they move away from the top of the liner, and the decrease in the jet velocity is more obvious than the slug velocity because the latter has a small value. The Gurney velocity method shows a continuous increase in the decreasing velocity of the jet parameters, whereas the proposed method displays an initial increase followed by a decrease.

From the velocity distribution curve of the jet shown in Fig. 7(b), it can be observed that there is a reverse velocity gradient in the jet, confirming the theory first discovered and proposed by Kiwan and Wisniewski (1972). The elements near the top of the liner do not have enough time to accelerate to the final velocity before collapsing, resulting in a slower collapse velocity and jet velocity. On the other hand, elements in the intermediate liner have higher collapse velocity due to a longer acceleration distance. So, the velocity gradient of the jet near the top is negative relative to the position of the liner. In addition, microelements near the top accumulate mass to form the head of the jet, which has been validated through experiments conducted by Carleone, Jameson, Chou, and others.

Two theoretical solutions and numerical simulation results were compared for collapse and jet velocities. Fig. 8 shows that the velocity distribution calculated by the proposed method agreed well with the simulation results and outperformed the Gurney velocity method.

3. Numerically assisted research

3.1. Numerical simulation model

Taking the DP46RDX42-Y perforating charge as an example, Fig. 9 shows the calculation model, which consists of four parts: shell, explosive, liner, and air. The outside diameter of the perforating projectile is 52 mm, the internal diameter of the perforating charge is 46 mm, the height is 62 mm, and the depth of the liner pressed into the shell is 2 mm. 320 different perforating charges were created by changing the liner thickness, cone angle, material, and explosive type under the same shell material. Table 2 displays the specific values of the four variables.

The calculation model was simulated using LS-DYNA software. The numerical algorithm was ALE, where the shell and liner are Lagrangian meshes, while the explosive and air are Euler meshes. The symmetric boundary was set for the symmetric axis, and a non-reflection boundary for a model boundary to avoid reflection impact on the calculation results.

3.2. Material model and parameters

3.2.1. Explosive

Explosives studied in this paper are TNT, OCTOL, B explosive, C-1 explosive, and 8701 explosive; the high-energy explosive model and JWL equation of state are used. The pressure generated by explosive detonation products can be expressed as (Walters and Zukas, 1989):

$$p = A\left(1 - \frac{\omega}{R_1 V}\right)e^{-R_1 V} + B\left(1 - \frac{\omega}{R_2 V}\right)e^{-R_2 V} + \frac{\omega E_0}{V} \tag{35}$$

where A, B, R_1, R_2, and ω are material parameters; E_0 is the specific internal energy; V is the relative volume. The specific material parameters are shown in Table 3.

3.2.2. Liner and shell

The liner and shell are made of metal materials and modeled by the Johnson-Cook model. The yield stress can be expressed as (Jonhson and Cook, 1983):

Table 3
Parameters of constitutive model and equation of state of explosives.

Parameter	TNT (Zhang et al., 2022)	OCTOL (Huang et al., 2020)	B explosive (Xu et al., 2019b)	C-1 explosive (Nan et al., 2015)	8701 explosive (Shi et al., 2023)
Density ρ_e, g/cm^3	1.63	1.82	1.60	1.93	1.72
Detonation velocity V_d, m/s	6930	8480	7980	9061	8500
Parameter A, GPa	373.77	748.6	524.23	1827.6	618.4
Parameter B, GPa	3.747	13.38	7.678	61.35	6.9
Parameter R_1	4.15	4.50	4.20	5.88	4.30
Parameter R_2	0.9	1.2	1.1	1.8	0.87
Parameter ω	0.35	0.38	0.34	0.30	0.38
Internal energy E_0, GJ/m^3	6.0	10.5	8.5	11.5	9.0

Table 4
Parameters of the constitutive model and state equation of metallic materials.

Parameter	Copper (Elshenawy et al., 2018)	Steel (Elshenawy and Li, 2013)	Titanium (Mu et al., 2022)	Tungsten (Mu et al., 2022)
Density ρ_m, g/cm^3	8.96	7.83	4.51	17.00
Shear modulus G, GPa	46	81.8	46	161
Elastic modulus E, GPa	115	210	110	411
Parameter A_1, GPa	0.09	0.792	1.111	1.506
Parameter B_1, GPa	0.292	0.510	0.106	0.177
Parameter C	0.025	0.014	0.025	0.016
Parameter n	0.31	0.26	0.29	0.12
Parameter m	1.09	1.03	1.10	1.00
Melting temperatures T_{melt}, K	1356	1793	1710	1723
Sound velocity c, m/s	3940	4569	5210	4029
Parameter S_1	1.49	1.49	1.62	1.24
Gruneisen coefficient γ_0	1.99	2.17	2.32	1.54

Table 5
Parameters of the equation of state of air.

Parameter	Density ρ_m, g/cm^3	C_0	C_1	C_2	C_4	C_5	C_6	Internal energy E_1, GPa
Value (Ma et al., 2022)	0.00125	0	0	0	0.4	0.4	0	0.00025

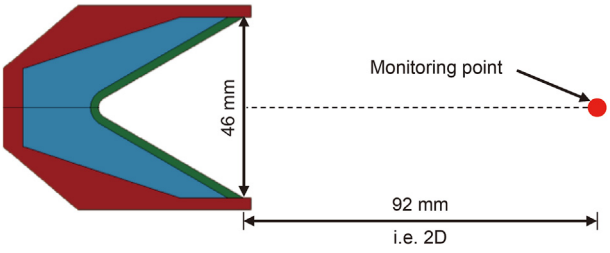

Fig. 10. The monitoring point located at 2D from the bottom of the liner.

$$\sigma_y = \left(A_1 + B_1\varepsilon_p^n\right)(1 + C\ln\dot{\varepsilon}^*)(1 - (T^*)^m) \tag{36}$$

where A_1, B_1, n, C, and m are all material constants determined by experiments; ε_p is the equivalent plas

tic strain; $\dot{\varepsilon}^*$ is the effective plastic strain rate; T^* is the homologous temperature, $T^* = (T - T_{room})/(T_{melt} - T_{room})$, where T, T_{room}, and T_{melt} are the experimental, room, and melting temperatures of the material, respectively.

The Gruneisen equation of state can describe the characteristics of metal material at a high strain rate. The pressure P in the compression and expansion state can be expressed as (Littlefield et al., 1997)

$$P = \begin{cases} \dfrac{\rho_0 c^2 \mu\left(1 + \left(1 - \dfrac{\gamma_0}{2}\right)\mu - \dfrac{a}{2}\mu^2\right)}{1 - (s_1 - 1)\mu - s_2\dfrac{\mu^2}{\mu+1} - s_3\dfrac{\mu^3}{(\mu+1)^2}} + (\gamma_0 + a\mu)E_1 & (\mu \geq 0) \\ \rho_0 c^2 \mu + (\gamma_0 + a\mu)E_1 & (\mu \leq 0) \end{cases} \tag{37}$$

where c is the intercept on the v_s-v_p curve; S_1, S_2, and S_3 are the coefficients of the slope of the v_s-v_p curve; γ_0 is the Gruneisen coefficient; a is the first-order volume correction of γ_0; $\mu = \rho/\rho_0 - 1$, ρ and ρ_0 are the deformed and initial material density; E_1 is the internal energy. The parameters are listed in Table 4.

3.2.3. Air

Use the linear polynomial equation to describe the equation of state of air. The pressure is expressed as:

$$p_a = C_0 + C_1\mu + C_2\mu^2 + C_3\mu^3 + \left(C_4 + C_5\mu + C_6\mu^2\right)E_1 \tag{38}$$

where E_1 is the internal energy per unit volume; C_0, C_1, C_2, C_3, C_4, C_5

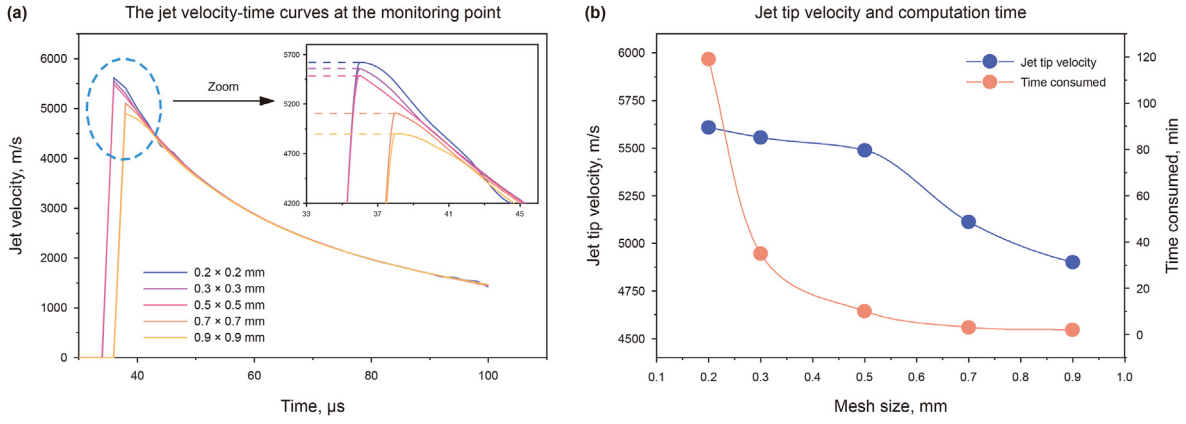

Fig. 11. Variation of jet velocity and computation time with mesh size.

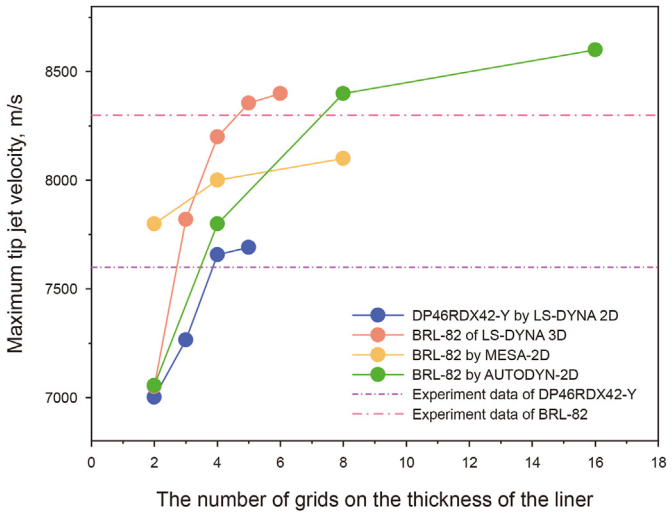

Fig. 12. The influence of liner thickness mesh number on maximum jet tip velocity.

and C_6 are coefficients of equation; μ is the relative volume, $\mu = \rho/\rho_0 - 1$, ρ/ρ_0 is the ratio of current density to initial density. The parameters are listed in Table 5.

3.3. Mesh sensitivity

It is widely recognized that the shape and density of the mesh used in simulations can impact the results obtained. Fine mesh simulation is generally more accurate but takes longer than coarse mesh simulation. Therefore, in the study of jet formation, researchers examine the variation of the jet characteristics with mesh density to investigate grid sensitivity.

3.3.1. Effect of mesh size on jet tip velocity

A shaped charge with 8701 explosive, a cone angle of 60°, a 2 mm thick copper liner, and a 3 mm thick steel shell was tested. The mesh sensitivity study in the jet formation was conducted using the methods of Elshenawy et al. (2018) and Agu et al. (2018). The study analyzed the effect of mesh size on jet tip velocity using five different square mesh sizes of 0.2, 0.3, 0.5, 0.7, and 0.9 mm. The monitoring point is situated at twice the charge diameter (92 mm) from the bottom of the liner to determine the jet velocity (see Fig. 10).

The velocity time history curves for five mesh sizes consistently show a trend and mostly overlap in the attenuation section, as seen in Fig. 11(a). As the mesh size decreases from 1.0 to 0.2 mm, the jet tip velocity gradually increases, with a convergence of the solution observed. Although the 0.2 × 0.2 mm^2 mesh size provides the most precise results, finishing the simulation takes almost twelve times longer than a 0.5 × 0.5 mm^2 mesh (See Fig. 11(b)). Surprisingly, the variation in jet tip velocity between them is only 130.9 m/s (2.3%). Consequently, simulations chose the 0.5 × 0.5 mm^2 mesh size, as the increased computational cost due to finer meshes cannot be compensated for through the accuracy of the obtained results.

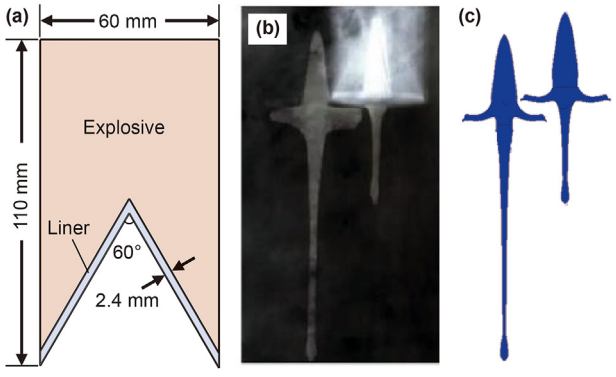

Fig. 13. Verification of numerical algorithm. (**a**) The geometric model; (**b**) pulsed X-ray photography (Ma et al., 2022); (**c**) numerical result.

Table 6
Comparison of numerical and experimental results.

Parameter	Measured by X-ray	Numerical results	Error
Length of jet at 26 μs, mm	41.1	42.0	2.1%
Length of jet at 42 μs, mm	77.6	78.5	1.6%
Velocity of jet tip, m/s	5276.2	5065.25	3.9%
Diameter of the jet, mm	4.18	4.09	2.1%

3.3.2. Effect of liner thickness grid number on jet velocity

To achieve an effective numerical simulation for the perforating charge model with 0.5 mm liner thickness in Tables 2, it is necessary to perform mesh refinement on critical areas, such as the liner. Thus, the shaped charge with the cone angles of 60°, thickness of 0.5 mm, and copper liner is numerically simulated to analyze the impact of liner thickness mesh number on jet velocity.

N is defined as the number of meshes on the thickness of the top liner, taking values 2, 3, 4 and 5. The edge lengths of the meshes in the critical areas of the corresponding charging and jet-forming channels are 0.25, 0.15, 0.125, and 0.1 mm, respectively. In Fig. 12, a comparison is made between the maximum jet top velocity at different mesh numbers and experimental results (Mu et al., 2022). Additionally, for the BRL-82 perforating charge, the maximum top velocity calculated by Los Alamos Laboratory using MESA-2D (Bolstad et al., 1992), Eer Gruel using AUTODYN-2D, and Liu et al. (2017) using LS-DYNA-3D under different *N* values and experimental results (Hancock, 2001) are also compared.

Fig. 12 shows that the jet tip velocity of both perforating charges increases gradually as *N* increases, and the velocity curve gradually tends to be constant. When the number of liner thickness meshes is greater than 4, the jet tip velocity of DP46RDX42-Y has a small error compared to the experimental result of 7600 m/s, which also proves the effectiveness of this numerical simulation method. Similarly, the jet tip velocity of BRL-82 is also close to the experimental result of 8300 m/s.

3.4. Verification of numerical algorithm

It has been confirmed in various studies that LS-DYNA is capable of simulating shaped charges (Wang et al., 2018). In explosion experiments, pulse X-ray photography has been widely used to measure the jet tip velocity and jet length. To ensure the reliability of numerical results, the study used the same geometric parameter model from reference (Ma et al., 2022), shown in Fig. 13(a). The numerical simulation is carried out based on the LS-DYNA combined with ALE, and the mesh size is set to 0.5 mm to ensure the accuracy of the calculation. Experiment and calculation use single-point detonation at the center of the explosive end face. The taken images of pulse X-ray photography at 26 and 42 μs are displayed in Fig. 13(b), while the numerical results are shown in Fig. 13(c). The results are listed in Table 6. The errors for jet velocity, length, and diameter are all less than 5%, indicating that this numerical method is highly effective in simulating the jet and can simulate experimental results.

Upon analyzing the efficacy and mesh convergence of the

Table 7
Correlation degree of each influencing factor.

Explosive material parameters	Influence factor	Liner material parameters	Influence factor
Density ρ_e, g/cm^3	0.69	Density ρ_m, g/cm^3	0.88
Detonation velocity V_d, m/s	0.88	Cone angle α, °	0.83
Parameter A, GPa	0.61	Thickness d, mm	0.83
Parameter B, GPa	0.49	Parameter m	0.76
Parameter R_1	0.76	Melting temperatures T_{melt}, K	0.74
Parameter R_2	0.73	Sound velocity c, m/s	0.77
Parameter ω	0.73	Parameter S_1	0.78
Internal energy E_0, GJ/m^3	0.59	Gruneisen coefficient γ_0	0.78

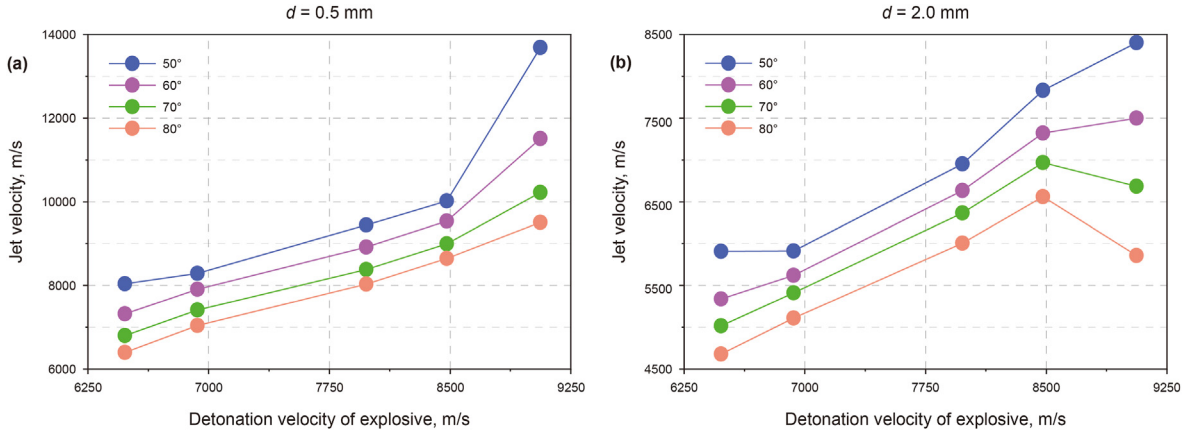

Fig. 14. Variation of jet velocity with detonation velocity of explosives (Numerical simulation results).

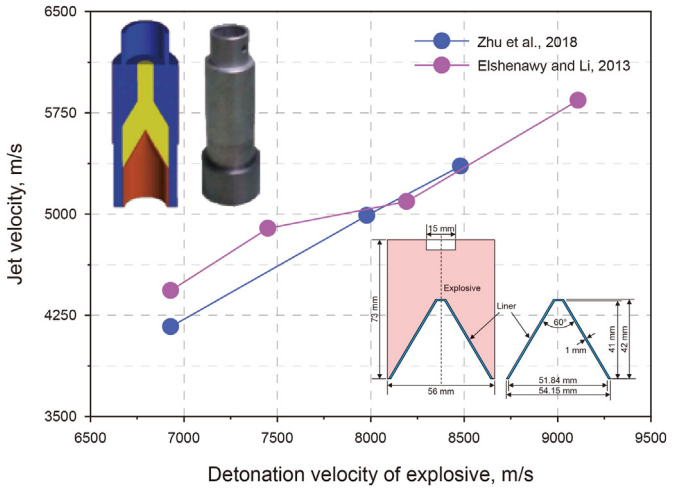

Fig. 15. Variation of jet velocity with detonation velocity of explosives (Experimental data) (Zhu et al., 2018; Elshenawy and Li, 2013).

numerical simulation, it was concluded that a mesh size of 0.5 × 0.5 mm^2 is optimal for this study. Furthermore, mesh refinement was conducted, with a particular emphasis on maintaining the number of meshes on the liner thickness at a minimum of four and employing a mesh size of 0.2 × 0.2 mm^2 for the central region where the jet traverses through explosives, liners, and air. This approach aims to improve the accuracy and effectiveness of numerical simulation of key areas of charge and jet formation channels.

3.5. Correlation analysis

The grey correlation theory was used to analyze the numerical simulation results, and the correlation degree between 22 parameters and jet head velocity was obtained, as shown in Table 7. The four material parameters that have the closest relationship with the jet velocity are the liner density ρ_m, the explosive detonation velocity V_0, the liner thickness d_m, and the liner cone angle α. The following chapters investigated the influence of these four main control parameters on jet velocity.

4. Results and discussion

4.1. Effect of parameters on jet velocity

4.1.1. Explosive detonation velocity

When using copper as the liner, the relationship between the jet top velocity and detonation velocity for different liner thicknesses is illustrated in Fig. 14. It is apparent that the jet top velocity increases proportionally to the explosion detonation velocity within a specific range, which agrees with the rules derived from experimental data in the literature (See Fig. 15). This proportional coefficient remains constant with the change in liner thickness. However, when the detonation velocity is too high, the jet velocity decreases as the explosive detonation velocity increases. The decrease is more significant for thicker liners. Therefore, appropriately using explosives with higher detonation velocity in perforating charges can considerably increase the jet velocity.

4.1.2. Liner thickness

Fig. 16 illustrates the correlation between jet top velocity and liner thickness for different line materials. The figure shows that when the explosive and liner materials are kept the same, the jet

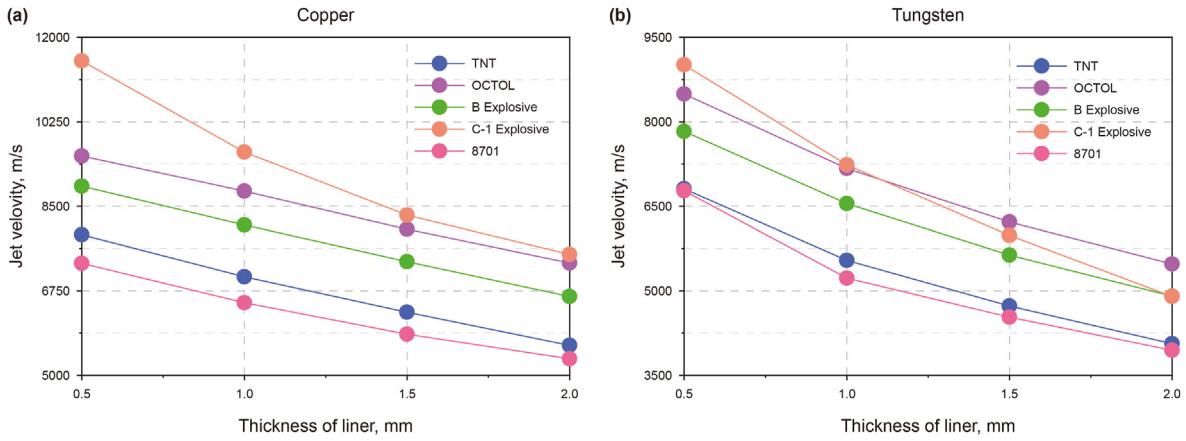

Fig. 16. Variation of jet velocity with liner thickness (Numerical simulation results).

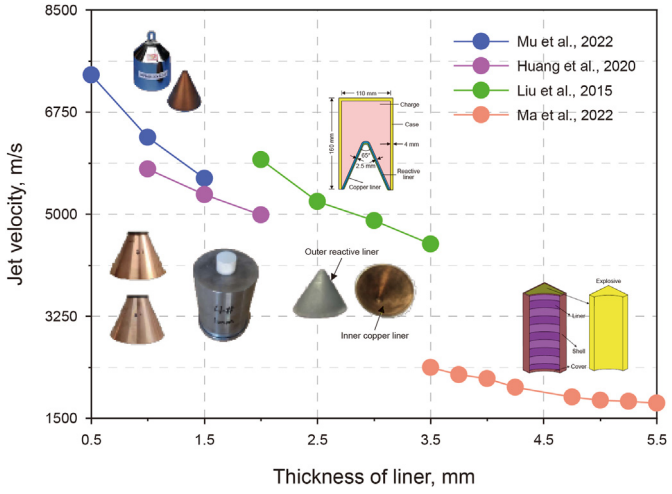

Fig. 17. Variation of jet velocity with liner thickness (Experimental data) (Mu et al., 2022; Ma et al., 2022; Huang et al., 2020; Liu et al., 2015).

top velocity decreases proportionally as the liner thickness increases. This correlation is consistent with experimental data discussed in Fig. 17. Notably, the proportional coefficient is less influenced by the explosive material and more by the liner material. Using a thinner liner in perforating charges can significantly improve the jet velocity.

4.1.3. Liner cone angle

Fig. 18 shows the relationship between the jet top velocity and the liner cone angle for different line materials. The graph demonstrates that as the thickness of the liner increases, the jet top velocity decreases proportionally. This decrease is not significantly influenced by the explosive or liner material, which is also supported by experimental data presented in Fig. 19. The graph suggests that using liners with a smaller cone angle in perforating charges can significantly improve the jet velocity.

4.1.4. Liner material density

When the explosive material is specified as 8701, Fig. 20 shows the relationship between the jet top velocity and liner material density for different liner thicknesses. It can be seen that the jet top velocity decreases proportionally as the liner material density increases, which is in line with the rules derived from experimental data in the literature (as shown in Fig. 21). This decrease is more significant for thicker liners. So, using a liner with a higher density in perforating charges can significantly increase the jet velocity.

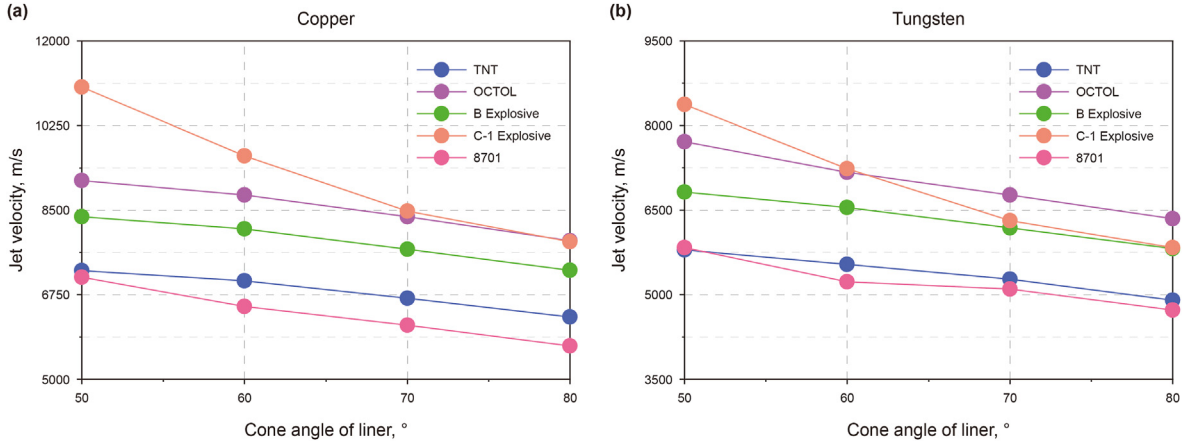

Fig. 18. Variation of jet velocity with cone angle (Numerical simulation results).

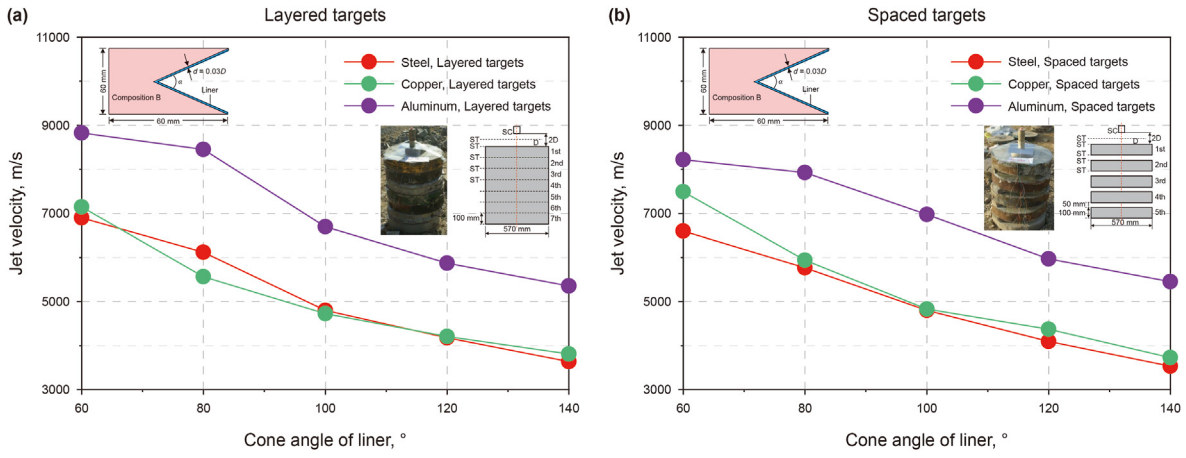

Fig. 19. Variation of jet velocity with cone angle (Experimental data) (Wang et al., 2018).

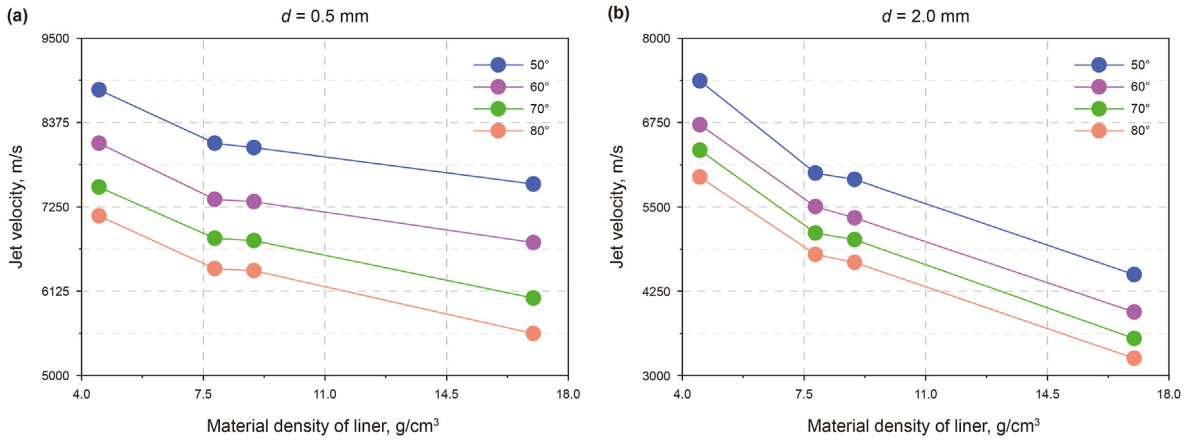

Fig. 20. Variation of jet velocity with liner density (Numerical simulation results).

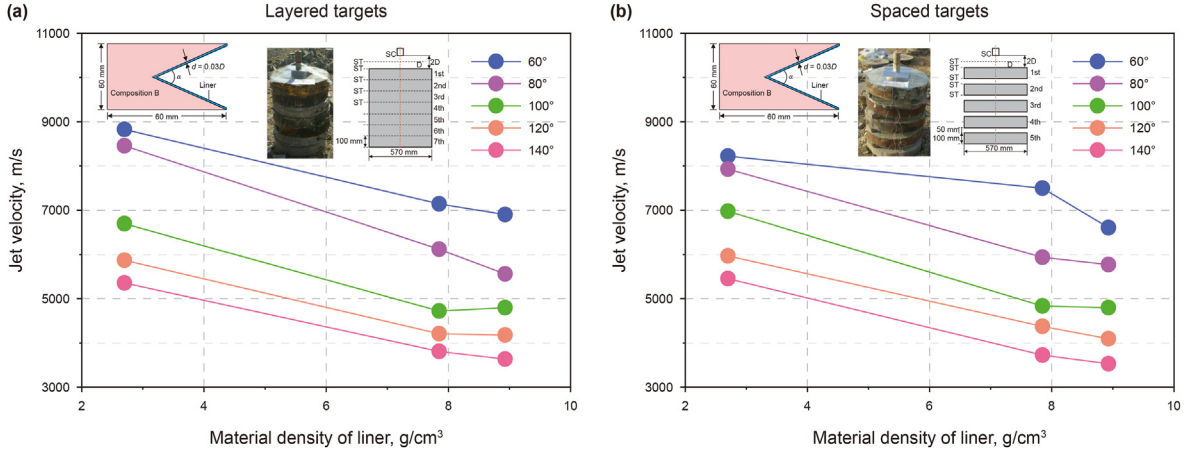

Fig. 21. Variation of jet velocity with liner density (Experimental data) (Wang et al., 2018).

4.2. Verification of proposed calculation method

4.2.1. Comparison of numerical simulation results

The article compares the results obtained from numerical simulations with the calculations using the Gurney formula and the improved decomposition velocity method. Fig. 22 shows that the improved method is more accurate in determining the jet velocity than the traditional Gurney formula. The calculation accuracy for the traditional model is 58.02%, while the improved model has an accuracy of 92.17%, an increase of 34.15% in accuracy. The proposed method has the highest accuracy for explosives with a detonation velocity of 8701 and the lowest for C-1 explosives. Therefore, the

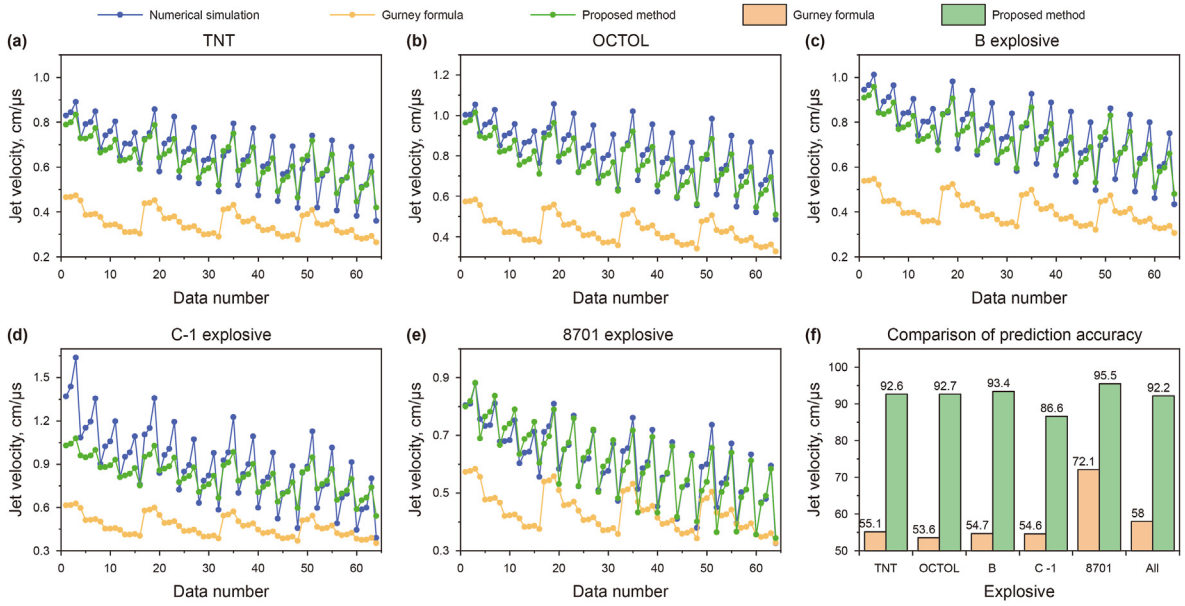

Fig. 22. Comparison between the calculated and actual value of jet velocity obtained by two methods.

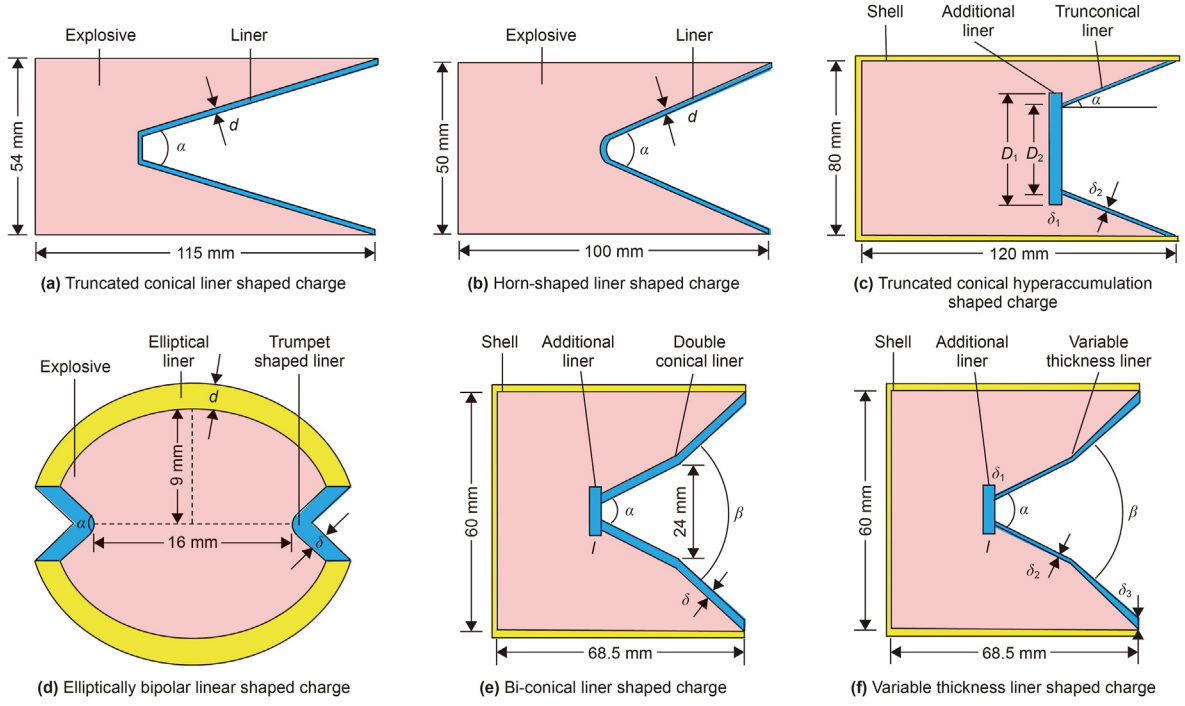

Fig. 23. Schematic diagrams of geometric models of different perforating charges.

method is more suitable for perforating charges with low detonation velocity.

4.2.2. Comparison of literature data

To examine the universality of the proposed method, the jet velocities generated by various perforating charges mentioned in literature (Huang et al., 2020; Lei et al., 2022; Ge et al., 2023; Wu et al., 2022; Lei, 2019) are taken as reference values for validation. The initiation point of the numerical model in all five references is positioned at the midpoint of the explosive, as illustrated in Fig. 23.

The method proposed in Section 2 for calculating jet velocity is based on shelled perforating charges with a conical liner such as DP46RDX42-Y. The method needs to be modified to calculate other perforating charges.

4.2.2.1. Truncated conical and horn-shaped liner. Fig. 23(a) and (b) show that the top of the truncated conical and horn-shaped liner is small enough to have a negligible impact on the jet velocity. Therefore, they can be considered as conical liners. Moreover, as long as the relevant parameters of the shell are set to zero and the formula, and other parameters remain unchanged, the improved method can be used to calculate the jet velocity of the shell-free

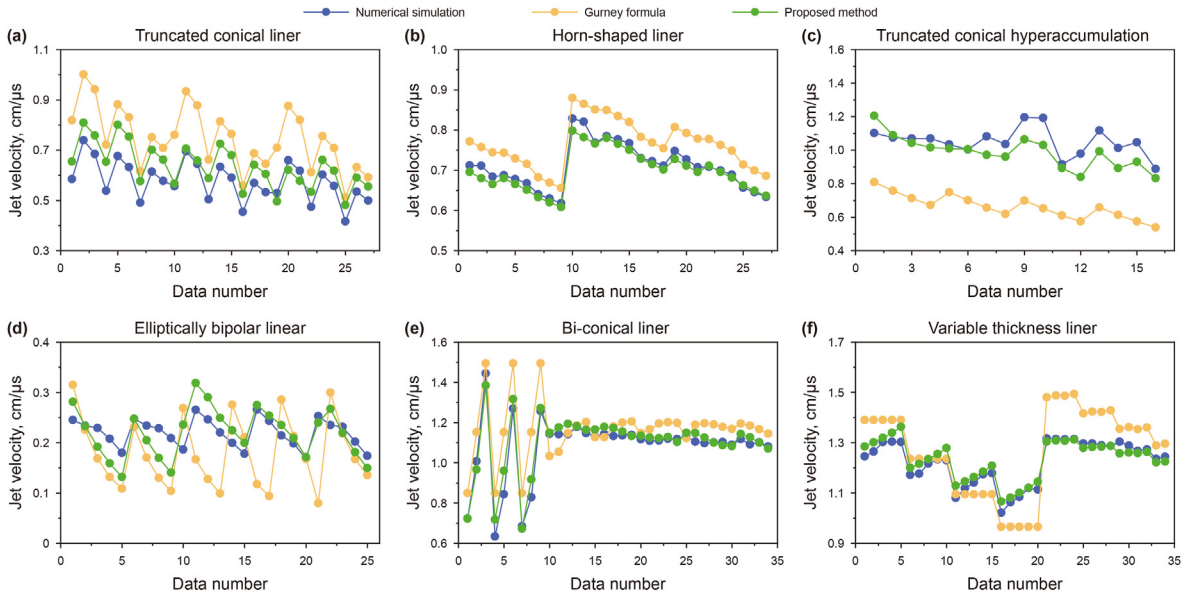

Fig. 24. Comparison between the literature data and the calculated results using two methods.

perforated charge.

4.2.2.2. Truncated conical hyperaccumulation-shaped charge. Fig. 23(c) shows a truncated conical hyperaccumulation-shaped charge consisting of an additional liner and a truncated conical liner. According to existing numerical simulation results, this structure can significantly enhance the effective mass and jet velocity, with the highest jet velocity observed at the point where the two liners connect. Therefore, it is necessary to calculate the two peak jet velocities separately and then add them up to obtain the final peak jet velocity. Note that when estimating the collapse velocity of the additional liner, only the axial charge component caused by the plate acceleration should be considered due to its cone angle of 90°.

4.2.2.3. Elliptically bipolar liner shaped charge. The elliptically bipolar liner shaped charge in Fig. 23(d) can be divided into an elliptical and a horn-shaped liner. The peak jet velocity of the perforating charge occurs at the center point of the trumpet-shaped liner, which is symmetrical about the vertical axis. The horn-shaped liner can be considered a conical liner, while the elliptical charge liner can be regarded as the shell of a perforating charge. Therefore, the elliptical bipolar linear charge is simplified as the shelled perforating charge with a conical liner for calculation.

4.2.2.4. Bi-conical liner. In Fig. 23(e), the bi-conical liner can be divided into an additional and two conical liners with varying cone angles. As per the results of numerical simulations in the literature, the structure exhibits a higher jet velocity and liner utilization rate. The method used for calculating the jet velocity can be referred to in the case of truncated conical hyperaccumulation-shaped charges.

4.2.2.5. Variable thickness liner. Fig. 23(f)shows a variable thickness liner shaped charge. The liner can be divided into an additional and variable-thickness liner. If the top of the liner is thin, the bottom is thick, and the thickness change rate is appropriate, then the resulting jet will have a higher velocity. The velocity of the jet can be calculated by using the methods of truncated conical hyperaccumulation and bi-conical shaped charges.

Fig. 24 compares the predicted values of the two methods and the target values of jet velocity. The traditional Gurney velocity method and the improved decomposition velocity method were studied on six different perforating shaped charges. It is observed that the predicted results of the proposed method are closer to the actual values in the five literatures.

According to Table 8, the improved method has a higher accuracy rate than the traditional method. The accuracy percentages range from 88.16% to 98.95%. The proposed method is more appropriate for horn-shaped or conical liners than truncated conical liners.

Table 8
Comparison of prediction accuracy.

Perforating charges	Accuracy, %	
	Gurney formula	Proposed method
Truncated conical liner	71.1	88.2
Horn-shaped liner	92.2	98.3
Truncated conical hyperaccumulation	63.1	92.5
Elliptically bipolar liner	67.9	86.9
Bi-conical liner	93.8	97.7
Variable thickness liner	82.9	96.1

5. Conclusions

Theoretical and numerical investigations for the velocity of the jet formed by shaped charges with different conditions are present in this paper. Based on the unsteady PER theory and the improved calculation method for collapse velocity, a new method for calculating the jet velocity of the shaped charge is proposed. Using the nonlinear finite element software LS-DYNA combined with the ALE techniques, a series of numerical simulations are carried out to analyze the influence of the different characteristic parameters on the jet velocity and verify the feasibility of the improved method. The main conclusions obtained are as follows:

(1) Taking into account elements like the liner, shell, explosive, and charge structure, the method presented in this paper provides a quick and effective approach to determine both

the liner collapse velocity and the jet tip velocity. This contributes significantly to optimizing the structural design of perforated charges and refining the computation of jet penetration depth.

(2) The key material parameters impacting jet velocity are liner density, explosive detonation velocity, liner thickness, and cone angle. According to findings from numerical simulation and experimental results in literature, it is evident that choosing explosives with higher detonation velocities and liners with reduced density, cone angles, and thickness can notably improve jet velocity. This insight is crucial for guiding the design of perforated charges structures to achieving heightened jet velocities.

(3) The numerical simulation results show that the improved method can achieve more fast and accurate prediction of metal jet velocity than the traditional Gurney formula, with an accuracy increase of 34.15%. In addition, the proposed method is also suitable for the perforating charges with different liner shapes, which is universal and flexible.

CRediT authorship contribution statement

Kun Jiang: Writing – original draft, Validation, Software, Methodology, Investigation, Data curation. **Shou-Chun Deng:** Writing – review & editing, Supervision, Resources, Funding acquisition. **Hai-Bo Li:** Resources, Funding acquisition.

Declaration of competing interest

The authors declare that they have no known competing financial interests or personal relationships that could have appeared to influence the work reported in this paper.

Acknowledgments

The study was supported by the National Key R&D Program of China (2020YFA0711802). The authors would like to express their deepest gratitude for the generous support.

References

Agu, H.O., Hameed, A., Appleby-Thomas, G.J., 2018. Application of shell jetting analysis to determine the location of the virtual origin in shaped charges. Int. J. Impact Eng. 122, 175–181. https://doi.org/10.1016/j.ijimpeng.2018.04.014.

Allison, F.E., Vitali, R., 1963. A New Method of Computing Penetration Variables for Shaped Charge Jets. Army Ballistic Research Lab Aberdeen Proving Ground Md.

Ayisit, O., 2008. The influence of asymmetries in shaped charge performance. Int. J. Impact Eng. 35 (12), 1399–1404. https://doi.org/10.1016/j.ijimpeng.2008.07.027.

Birkhoff, G., MacDougall, D.P., Pugh, E.M., Taylor, S.G., 1948. Explosives with lined cavities. J. Appl. Phys. 19 (6), 563–582. https://doi.org/10.1063/1.1698173.

Bolstad, J.W., Mandell, D.A., Mendius, P.W., 1992. Calculation of a Shaped Charge Jet using MESA-2D and MESA-3D Hydrodynamic Computer Codes. Los Alamos National Lab.

Chanteret, P.Y., 1983. An analytical model for metal acceleration by grazing detonation. In: Proc. 7th Inf. Sympo. Ballistics, pp. 515–524.

Chen, C., Wang, X.M., Li, W.B., Dong, X.L., 2015. Effect of matching of detonation waveform with liner configuration on the rod-like jet formation. Explos. Shock Waves 35 (6), 812–819. https://doi.org/10.11883/1001-1455(2015)06-0812-08.

Chen, J., Feng, D., Deng, S., Peng, C., Lien, F., 2020. GPU-accelerated smoothed particle hydrodynamics modeling of jet formation and penetration capability of shaped charges. J. Fluid Struct. 99, 103171. https://doi.org/10.1016/j.jfluidstructs.2020.103171.

Chen, Q.Y., Liu, K.X., 2012. A high-resolution Eulerian method for numerical simulation of shaped charge jet including solid–fluid coexistence and interaction. Comput. Fluids 56, 92–101. https://doi.org/10.1016/j.compfluid.2011.11.017.

Chou, P.C., Flis, W.J., 1986. Recent developments in shaped charge technology. Propell., Explos., Pyrotech. 11 (4), 99–114. https://doi.org/10.1002/prep.19860110402.

Chou, P.C., Carleone, J., Karpp, R.R., 1976. Criteria for jet formation from impinging shells and plates. J. Appl. Phys. 47 (7), 2975–2981. https://doi.org/10.1063/1.323038.

Chou, P.C., Carleone, J., Flis, W.J., Ciccarelli, R.D., Hirsch, E., 1983. Improved formulas for velocity, acceleration, and projection angle of explosively driven liners. Propellants, Explos. Pyrotech. 8 (6), 175–183. https://doi.org/10.1002/prep.830080602.

Chou, P.C., Flis, W.J., Forsyth, C.M., 1986. A simplified model of jet formation in hemispherical shaped charges. In: Proc. 9th Inf. Sympo. Ballistics.

Curtis, J.P., Kelly, R.J., 1994. Circular streamline model of shaped-charge jet and slug formation with asymmetry. J. Appl. Phys. 75 (12), 7700–7709. https://doi.org/10.1063/1.356601.

Elshenawy, T., Li, Q., 2013. Influences of target strength and confinement on the penetration depth of an oil well perforator. Int. J. Impact Eng. 54, 130–137. https://doi.org/10.1016/j.ijimpeng.2012.10.010.

Elshenawy, T., Elbeih, A., Klapötke, T.M., 2018. A numerical method for the determination of the virtual origin point of shaped charge jets instead of using flash X-ray radiography. J. Energetic Mater. 36, 127–140. https://doi.org/10.1080/07370652.2017.1324532.

Ge, C., Qu, Z., Wang, J., Hu, D., Zhang, Y., 2023. Study on jet formation behavior and optimization of trunconical hypercumulation shaped charge structure. Def. Technol 21, 196–206. https://doi.org/10.1016/j.dt.2022.09.017.

Gurney, R.W., 1943. The initial velocity of fragment from bombs, shells and grenades. BRL Report. https://doi.org/10.21236/ada289704.

Hancock, S.L., 2001. An extension of the umin model for cutoff of high precision jets. Int. J. Impact Eng. 26 (1–10), 289–298. https://doi.org/10.1016/S0734-743X(01)00095-1.

Hirsch, E., 1979. A simple representation of the Pugh, Eichelberger, and Rostoker solution to the shaped charge jet formation problem. J. Appl. Phys. 50 (7), 4667–4670. https://doi.org/10.1063/1.326576.

Hu, F., Wu, H., Fang, Q., Liu, J., Liang, B., Kong, X., 2017. Impact performance of explosively formed projectile (EFP) into concrete targets. Int. J. Impact Eng. 109, 150–166. https://doi.org/10.1016/j.ijimpeng.2017.06.010.

Huang, H.X., Zhang, H.S., Zhang, F., Yue, X.Y., Wang, M., 2020. Prediction method of shaped energy jet velocity based on BP artificial neural network. J. Gun Launch. Control 41 (1), 61–65. https://doi.org/10.19323/j.issn.1673-6524.2020.01.012.

Jin, Z., Zhang, W.W., 2020. Finite element modeling of the shaped charge jet and design of the reusable perforating gun. Petrol. Sci. 17 (5), 1389–1399. https://doi.org/10.1007/s12182-020-00468-4.

Jonhson, G.R., Cook, W.H., 1983. A constitutive model and data for metal subjected to large strains, high strain rates and high temperature. In: Proc. 7th Inf. Sympo. Ballistics, pp. 541–547.

Kiwan, A.R., Wisniewski, H., 1972. Theory and computations of collapse and jet velocities of metallic shaped charge liners. https://doi.org/10.21236/ad0907161.

Kolpakov, V., Kudyukov, N., Ladov, S., Nikolskaya, Y.M., Fedorov, S., 2018. The using of the shaped charges for destruction of ice cover. IOP Conf. Ser. Earth Environ. Sci. 193, 012039. https://doi.org/10.1088/1755-1315/193/1/012039.

Lei, F.C., 2019. The Deep Study of Shaped Charge Jet and Penetration under the New Shaped Charge Structure. Master's Thesis. Xi'an University of Technology, Xi'an.

Lei, J.Y., Wang, L.X., Kou, P.F., Xue, B., 2022. Study on the jet velocity prediction method based on the Kriging Model. Chin. J. Explos. Propellants 45 (5), 730–734. https://doi.org/10.14077/j.issn.1007-7812.202205028.

Littlefield, D.L., Anderson, C.E., Partom, Y., Bless, S.J., 1997. The penetration of steel targets finite in radial extent. Int. J. Impact Eng. 19 (1), 49–62. https://doi.org/10.1016/S0734-743X(96)00001-2.

Liu, H., Men, J., Jiang, J., Wang, S., 2017. Verification and validation for numerical simulation rules of the shaped charge based on LS-DYNA 3D. Trans. Beijing Inst. Technol. 37 (s2), 173–177+182.

Liu, C.L., Chen, L., Liu, D.Y., Yan, K., 2015. Effects of cone angles or thicknesses of liner on shaped charge jet velocity. Trans. Beijing Inst. Technol. 35 (s2), 86–89. https://doi.org/10.15918/j.tbit1001-0645.2015.S2.021.

Liu, J., Guo, X., Liu, Z., Liu, X., Liu, Q., 2018. Pressure field investigation into oil&gas wellbore during perforating shaped charge explosion. J. Petrol. Sci. Eng. 172, 1235–1247. https://doi.org/10.1016/j.petrol.2018.09.068.

Ma, S., Zhang, X., Qiu, X., 2009. Comparison study of MPM and SPH in modeling hypervelocity impact problems. Int. J. Impact Eng. 36 (2), 272–282. https://doi.org/10.1016/j.ijimpeng.2008.07.001.

Ma, T., Liu, J., Wang, Q., 2022. Influence of shaped charge structure parameters on the formation of linear explosively formed projectiles. Def. Technol 18 (10), 1863–1874. https://doi.org/10.1016/j.dt.2021.08.005.

Mu, G.Y., Luo, N., Shen, T., Liang, H.L., Cai, Y.B., Zhai, C., 2022. Mechanism of damage-induced fracture formation in shale reservoir penetrated by shaped charge jet. Explos. Shock Waves 43 (3), 85–101. https://doi.org/10.11883/bzycj-2022-0182 (in Chinese).

Nan, Y., Jiang, J., Wang, S., 2015. JWL Equation of state of detonation product for CL-20 based pressed composite explosive. Chin. J. Eng. Mater. 23 (6), 516–521. https://doi.org/10.11943/j.issn.1006-9941.2015.06.002.

Nie, B., Li, J., Zhang, H., 2014. Interaction between reflected shock and bubble in near-wall underwater explosion. Procedia Eng. 126, 344–348. https://doi.org/10.1016/j.proeng.2015.11.205.

Perez, E., Fauquignon, C., Chanteret, P., 1977. Fundamental studies of shaped charge mechanisms. In: Proc. 3rd Inf. Sympo. Ballistics.

Pugh, E.M., Eichelberger, R.J., Rostoker, N., 1952. Theory of jet formation by charges with lined conical cavities. J. Appl. Phys. 23 (5), 532–536. https://doi.org/10.1063/1.1702246.

Shen, F., Wang, H., Yuan, J.F., Tian, Q.Z., 2013. A simple estimation method for gurney coefficient of explosive. Chin. J. Explos. Propellants 36 (6), 36–38. https://doi.org/10.14077/j.issn.1007-7812.2013.06.006.

Shi, J., Huang, Z., Zu, X., Xiao, Q., 2023. Cohesiveness and penetration performance of jet: theoretical, numerical, and experimental studies. Int. J. Impact Eng. 175, 104543. https://doi.org/10.1016/j.ijimpeng.2023.104543.

Sun, C.J., Lu, Y.G., Li, H.M., 2009. Model of theoretical calculation of shaped charge with modified P-E-R theory. J. Project., Rockets, Missiles Guid. 29 (4), 99–102.

Walters, W.P., Zukas, J.A., 1989. Fundamentals of Shaped Charges. Wiley Interscience Publication. https://doi.org/10.1002/prep.19890140510.

Wang, C., Xu, W., Chung Kim Yuen, S., 2018. Penetration of shaped charge into layered and spaced concrete targets. Int. J. Impact Eng. 112, 193–206. https://doi.org/10.1016/j.ijimpeng.2017.10.013.

Wu, B., Xu, S., Meng, G., Cui, Y., 2022. Research on structural parameter optimization of elliptical bipolar linear shaped charge based on machine learning. Heliyon 8 (10), e10992. https://doi.org/10.1016/j.heliyon.2022.e10992.

Xiao, Q., Huang, Z., Jia, X., Zu, X., Zhu, Q., 2017. Shaped charge penetrator into soil–concrete double-layered target. Int. J. Impact Eng. 109, 302–310. https://doi.org/10.1016/j.ijimpeng.2017.07.003.

Xu, L., Tian, Y., Liu, X., Wang, S., 2023a. Numerical investigation on jet penetration capacity of hypervelocity shaped charge in underwater explosion. Ocean Eng. 281, 114668. https://doi.org/10.1016/j.oceaneng.2023.114668.

Xu, M.W., Huang, Z.X., Zu, X.D., Xiao, Q.Q., Jia, X., Ma, B., 2023b. Mesoscale simulation of shaped charge iet forming and free flight based on B-spline and domain interpolation material point method. Int. J. Impact Eng. 181, 104728. https://doi.org/10.1016/j.ijimpeng.2023.104728.

Xu, W.L., Wang, C., Chen, D., 2019a. Formation of a bore-center annular shaped charge and its penetration into steel targets. Int. J. Impact Eng. 127, 122–134. https://doi.org/10.1016/j.ijimpeng.2019.01.008.

Xu, W., Wang, C., Chen, D., 2019b. The jet formation and penetration capability of hypervelocity shaped charges. Int. J. Impact Eng. 132, 103337. https://doi.org/10.1016/j.ijimpeng.2019.103337.

Yan, Y., Guan, Z., Yan, W., Wang, H., 2020. Mechanical response and damage mechanism of cement sheath during perforation in oil and gas well. J. Pet. Sci. Eng. 188, 106924. https://doi.org/10.1016/j.petrol.2020.106924.

Yavuz, M.S., Yıldırım, R.O., Serin, N., 2012. Numerical and experimental investigation of jet formation and particulation in shaped charges with tulip-like steel liners. Procedia Eng. 58, 608–616. https://doi.org/10.1016/j.proeng.2013.05.070.

Yin, Y., Sun, Q., Zou, B., Mu, Q., 2021. Numerical study on an innovative shaped charge approach of rock blasting and the timing sequence effect in microsecond magnitude. Rock Mech. Rock Eng. 54 (9), 4523–4542. https://doi.org/10.1007/s00603-021-02516-w.

Zhang, H., Zheng, Y., Yu, Q., Ge, C., Su, C., Wang, H., 2022. Penetration and internal blast behavior of reactive liner enhanced shaped charge against concrete space. Def. Technol 18 (6), 952–962. https://doi.org/10.1016/j.dt.2021.04.011.

Zhang, Z., Wang, L., Ming, F., Silberschmidt, V.V., Chen, H., 2017. Application of Smoothed Particle Hydrodynamics in analysis of shaped-charge jet penetration caused by underwater explosion. Ocean Eng. 145, 177–187. https://doi.org/10.1016/j.oceaneng.2017.08.057.

Zhu, Q., Huang, Z., Xiao, Q., Zu, X., Jia, X., 2018. Theoretical and experimental study of shaped charge jet penetration into high and Ultra-high strength concrete targets. Int. J. Impact Eng. 122, 431–438. https://doi.org/10.1016/j.ijimpeng.2018.04.010.